

Electric-Field and Doping-Induced Non collinear Magnetic Interactions in Monolayer Ti_2Si

Dimple Rani,^{1,*} Gayatri Panda,¹ Subrata Jana,² and Prasanjit Samal¹

¹*School of Physical Sciences, National Institute of Science Education and Research,
An OCC of Homi Bhabha National Institute, Jatni 752050, India*

²*Institute of Physics, Faculty of Physics, Astronomy and Informatics,
Nicolaus Copernicus University in Toruń, ul. Grudziądzka 5, 87-100 Toruń, Poland*

Two-dimensional (2D) silicides are an emerging class of materials whose magnetic and relativistic properties remain largely unexplored. Using first-principles calculations, we investigate how electric-field modulation and transition-metal doping influence the magnetic exchange, magnetocrystalline anisotropy, and antisymmetric Dzyaloshinskii–Moriya interaction (DMI) in monolayer Ti_2Si . Pristine Ti_2Si is a dynamically stable ferromagnetic metal with in-plane anisotropy and centrosymmetric bonding, which suppresses DMI even under strong perpendicular electric fields. To overcome this symmetry constraint, we introduce Pt and Co substitution at Ti sites. Co enhances the magnetic exchange, whereas Pt provides strong spin orbit coupling (SOC), and the combined chemical asymmetry breaks inversion symmetry sufficiently to induce a sizable DMI. A Wannier-based tight-binding model captures the orbital-resolved superexchange pathways and reveals a clear hierarchy between a weak Si-mediated channel and a dominant Pt-mediated interlayer channel. First Principle calculations confirm that the Pt-assisted pathway governs the magnitude and sign of the total DMI. Among all configurations, $\text{Pt}_{0.5}\text{CoTi}_{0.5}\text{Si}$ exhibits the strongest chiral interaction, with its intralayer and interlayer contributions favoring opposite rotation senses, namely counterclockwise (CCW) and clockwise (CW). Our results establish chemically engineered Ti_2Si monolayers as a promising platform for realizing and tuning chiral magnetic textures in 2D silicides.

I. INTRODUCTION

Magnetic textures arise from the delicate balance between symmetric exchange interactions [1], magnetic anisotropy [2], and the antisymmetric Dzyaloshinskii–Moriya interaction (DMI) [3, 4]. The DMI stems from strong spin–orbit coupling (SOC) in systems lacking inversion symmetry and promotes chiral spin arrangements, giving rise to spin structures with nontrivial topology. In recent years, DMI-driven magnetic states have gained considerable attention due to the fundamental insights they offer into chiral magnetism and their promising implications for high-density, energy-efficient spintronic applications [5–7].

In recent years, two-dimensional (2D) magnetism has revealed a diverse range of materials capable of hosting DMI-driven spin textures [8–11]. Beyond the well-studied CrI_3 [12], Fe_3GeTe_2 [13], MnSe_2 [14], and FeTe_2 [15], long-range magnetic order has also been reported in layered halides such as CrBr_3 and CrCl_3 [16, 17], transition-metal phosphorus trichalcogenides (MPX_3 ; $\text{M} = \text{Mn, Fe, Ni}$; $\text{X} = \text{S, Se}$) [18], and metallic systems including monolayer VSe_2 [19] and NbSe_2 [20]. Transition-metal dichalcogenides (TMDs), in particular, provide a versatile platform for engineering chiral magnetism, where heavy-element substitution [21, 22], Janus engineering [e.g., $\text{Cr}_2\text{X}_3\text{Y}_3$ ($\text{X, Y} = \text{Cl, Br, I}$; $\text{X} \neq \text{Y}$) [23], MnXY ($\text{X, Y} = \text{S, Se, Te}$; $\text{X} \neq \text{Y}$) [24], and CrXTe ($\text{X} = \text{S, Se}$) [25]], or interfacing with high-SOC substrates such as Pt, W, and Ir [26–28] can significantly enhance the DMI.

2D silicides remain largely unexplored in the context of chiral magnetism and the DMI. While bulk and thin-film silicides have been widely studied for their electronic, catalytic,

and thermoelectric properties [29, 30], their magnetic behavior particularly spin orbit-driven effects has received comparatively little attention. Reported magnetic silicides such as GdSi_2 and TbSi primarily exhibit conventional magnetic ordering without evidence of chiral textures [31, 32]. Although recent theoretical work shows that heavy-metal incorporation or inversion-symmetry breaking in transition-metal systems can generate sizable DMI [7, 23], most demonstrations in silicides have been limited to bulk or epitaxial MnSi -based films [33, 34]. Whether monolayers or quasi-2D silicides can host DMI-driven chiral magnetism, where reduced dimensionality and interface-induced SOC may play a decisive role remains an open question. This gap is particularly compelling given the structural robustness of silicides, their compatibility with silicon technology, and their potential for enhanced SOC.

Titanium silicide (Ti_2Si) monolayers have recently been predicted to exhibit remarkable multifunctional properties, including intrinsic ferromagnetism, tunable electronic phases, and catalytic activity [35]. First-principles calculations indicate that Ti_2Si is dynamically stable and hosts local magnetic moments on Ti atoms arising from partially filled $3d$ orbitals [35]. The magnetic ordering and electronic character can be effectively tuned through strain, carrier doping, or chemical modification, enabling transitions between metallic, half-metallic, and semiconducting states [36]. Although Ti and Si possess relatively modest SOC, the Ti $3d$ states near the Fermi level provide a magnetic framework that can couple to external perturbations, breaking inversion symmetry and enabling the emergence of DMI and chiral spin textures.

In this work, we investigate monolayer Ti_2Si using first-principles calculations as a 2D transition metal silicide (TMS) platform for tunable magnetism and potential chiral spin states. We first examine the effect of an external perpendicular electric field (\vec{E}) on its magnetic anisotropy and exchange interactions. We then explore substitutional doping

* Corresponding author: dimple.rani@niser.ac.in

with Pt, to enhance SOC, and Co, to strengthen ferromagnetism, an approach known to promote sizable DMI in layered systems [37, 38]. Together, these two routes allow us to assess both field-induced magnetic modulation and doping-driven DMI, providing a comprehensive picture of the conditions under which Ti_2Si can sustain noncollinear and chiral magnetic configurations.

In addition, we construct a minimal Wannier-based tight-binding (TB) model [39, 40], which captures the SOC-induced superexchange pathways responsible for DMI and efficiently verifies the density functional theory (DFT) trends.

II. MODEL AND COMPUTATIONAL DETAILS

We investigate the 2D TMS compound Ti_2Si , which crystallizes in a tetragonal structure belonging to the centrosymmetric space group $P4/mmm$, with optimized lattice constants $a = b = 2.73$ with vacuum slab 20 Å. All first-principles calculations are performed within the framework of DFT using the VASP package [41]. The electron ion interactions are described using the projector augmented wave (PAW) method [42, 43], and the exchange correlation energy is treated within the generalized gradient approximation (GGA) of Perdew, Burke, and Ernzerhof (PBE) [44]. To account for on-site Coulomb interactions among Ti 3d states, we employ the DFT+ U method [35] in the Dudarev formulation [45] with an effective $U_{\text{eff}} = 2$ eV, which correctly reproduces the ground-state magnetic configuration of Ti_2Si monolayers. The plane-wave basis set is truncated at a kinetic energy cutoff of 420 eV, and Brillouin-zone integrations are performed using a Γ -centered $16 \times 16 \times 1$ Monkhorst–Pack k -point grid. Phonon dispersions are computed using the PHONOPY code [46] within the finite-displacement approach using 4×4 supercells to verify the dynamical stability of all structures.

Using a supercell approach, the DMI vectors (\vec{d}_{ij}) are evaluated through a three step procedure. First, full structural relaxations are performed to obtain the equilibrium interfacial geometry, with convergence thresholds of 10^{-6} eV in total energy and 0.001 eV/Å in forces. Second, the ground-state charge density is obtained by solving the Kohn–Sham equations without SOC. In the final step, SOC is introduced, and the self-consistent total energy is computed for different orientations of the magnetic moments using VASP’s constrained-magnetization method. This approach, previously employed to assess DMI in bulk frustrated and chiral-lattice magnets [47], is adapted here for the monolayer system. The DMI is extracted by enforcing opposite spin-rotation chiralities (clockwise and counterclockwise) in a 4×1 supercell for pristine Ti_2Si and a 4×2 supercell for Pt- and Co-doped structures. The resulting energy differences yield both the direction and magnitude of the DMI vectors with high accuracy.

To compute the orbital-resolved DMI, we construct a TB Hamiltonian from maximally localised Wannier functions (MLWFs) generated using the WANNIER90 package [39]. Our starting point follows the Anderson superexchange framework [48], later generalized by Moriya [49] and

Dzyaloshinskii [50] to include antisymmetric exchange in the presence of SOC. The Wannier-based TB Hamiltonian [51] reproduces the *ab initio* electronic structure and provides access to orbital resolved hopping parameters calculated using TBMODELS [52], which form the basis for evaluating symmetric and antisymmetric exchange interactions. In this formulation, the MLWFs serve as localized orbitals on both the magnetic cations and the ligand sites, naturally incorporating the underlying crystal symmetry and enabling a rigorous definition of orbital overlaps. SOC is explicitly included in the effective Hamiltonian, and interactions among all relevant nearest neighbours are considered. By analysing the complex hopping amplitudes between orbital pairs, the orbital-resolved DMI is obtained directly for Ti_2Si and its doped derivatives.

III. RESULTS AND DISCUSSIONS

A. Structural, Electronic, and Magnetic Properties

In this paper, we have investigated the monolayer Ti_2Si , shown in Fig. 1(a), which consists of a Ti–Si–Ti trilayer with a bond angle $\theta = 63^\circ$, indicating a slight deviation from ideal planarity. The phonon dispersion calculated using a 4×4 supercell [Fig. 1(b)] displays no imaginary frequencies throughout the Brillouin zone, confirming the dynamical stability of the Ti_2Si monolayer. The orbital-resolved DOS in Fig. 1(c) shows that the states near the Fermi level are mainly contributed by the Ti 3d orbitals, with noticeable hybridization from the Si 3p states. The exchange splitting of the Ti 3d orbitals produces a spin-polarized electronic structure, confirming that Ti_2Si behaves as an itinerant ferromagnetic metal. The total magnetic moment is about $1.43 \mu_B$ per unit cell, concentrated mostly on the Ti atoms, with the Si p orbitals contributing through an indirect superexchange pathway. To understand how Ti_2Si responds to external perturbations, we applied a perpendicular electric field (\vec{E}) and examined how it affects the electronic and magnetic properties.

In order to understand the magnetic interactions in Ti_2Si monolayers, we consider the generalized spin Hamiltonian,

$$H = \frac{1}{2} \sum_{i,j} J_{ij} \mathbf{S}_i \cdot \mathbf{S}_j + K_\mu \sum_i (S_i^z)^2 + \frac{1}{2} \sum_{i,j} \mathbf{d}_{ij} \cdot (\mathbf{S}_i \times \mathbf{S}_j), \quad (1)$$

where J_{ij} represents the isotropic Heisenberg exchange coupling, K_μ denotes the uniaxial single-ion anisotropy constant, and \mathbf{d}_{ij} is the Dzyaloshinskii–Moriya vector. The anisotropy term governs the preferred spin orientation, stabilizing out-of-plane alignment for $K_\mu > 0$ and in-plane orientation for $K_\mu < 0$. The DMI contribution encodes the antisymmetric exchange that favors chiral spin textures. To determine the preferred magnetic configuration, both ferromagnetic (FM) and antiferromagnetic (AFM) alignments were considered [Figs. 1(d)–(e)]. The Heisenberg exchange interaction parameter J was obtained from the total energy difference of FM and AFM (derived in Supplementary material Section II [53]) as shown in Fig. 1(f), J remains negative for electric fields in the

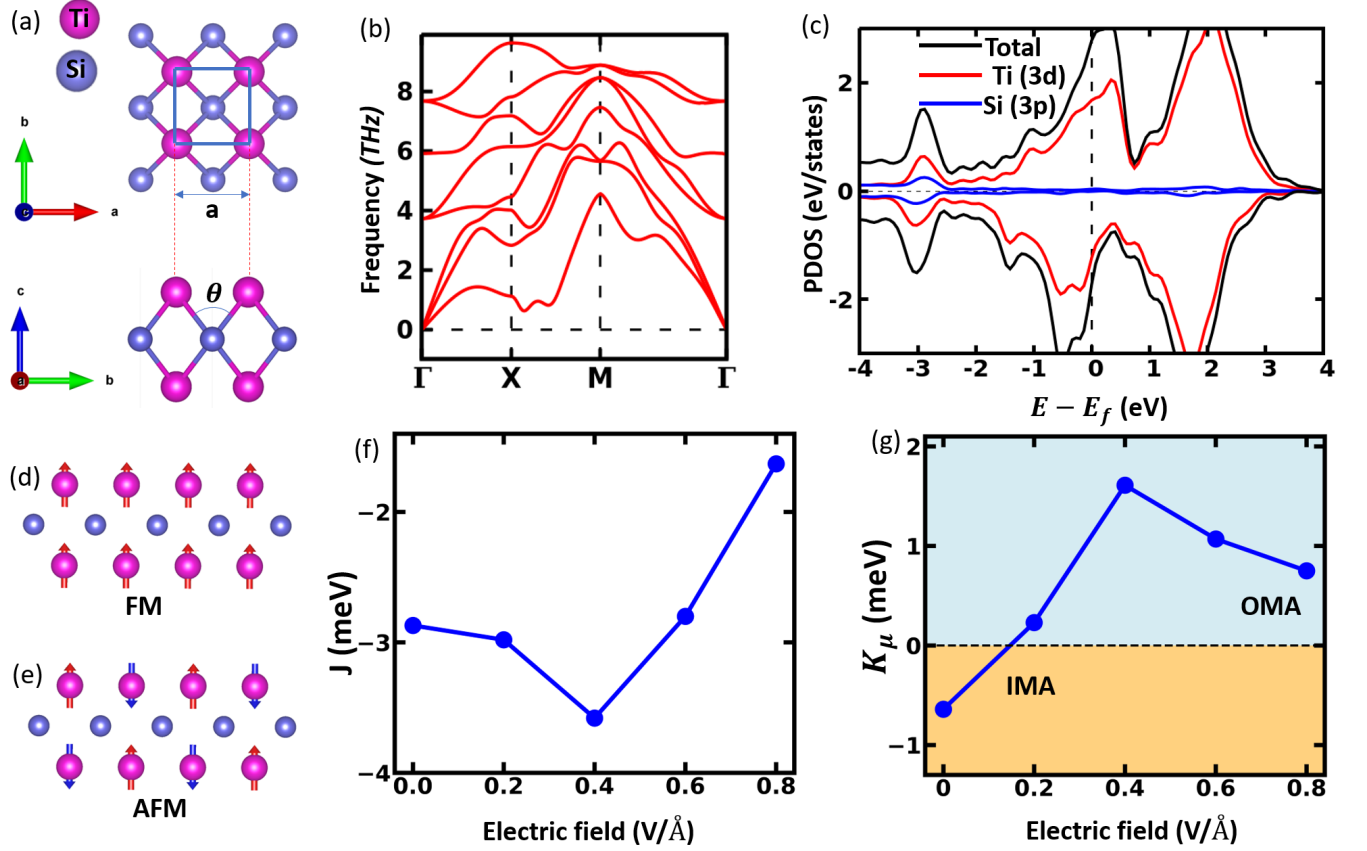


FIG. 1. (a) Top and side views of the Ti_2Si monolayer, where a denotes the lattice constant and θ represents the bond angle. (b) Phonon dispersion confirming the dynamical stability of the system. (c) Spin-polarized projected density of states (PDOS) of the Ti_2Si monolayer. (d) and (e) Schematic representations of the ferromagnetic and antiferromagnetic spin configurations, respectively. (f) Heisenberg exchange interaction parameter J as a function of external electric field. (g) Single-ion anisotropy as a function of external electric field, where the blue region indicates out-of-plane magnetic anisotropy (OMA) and the yellow region corresponds to in-plane magnetic anisotropy (IMA).

range 0–0.8 $\text{V}/\text{\AA}$, indicating the energetic preference for the FM state. The magnitude of $|J|$ exhibits a nonmonotonic variation with \vec{E} initially decreasing and then increasing reflecting field-induced modulation of the Ti– d and Si– p orbital overlap that governs the superexchange interaction. The strongest FM coupling is observed near 0.4 $\text{V}/\text{\AA}$, beyond which the interaction weakens.

The single-ion magnetic anisotropy constant (K_μ) is evaluated as

$$K_\mu = E_{\parallel} - E_{\perp}, \quad (2)$$

where E_{\parallel} and E_{\perp} denote the total energies with magnetization oriented in-plane and out-of-plane, respectively. A positive K_μ indicates an easy-axis anisotropy along the out-of-plane direction, which is favorable for skyrmion formation. As shown in Fig. 1(g), K_μ exhibits strong field dependence: at zero electric field, $K_\mu < 0$ corresponds to an in-plane magnetic anisotropy (IMA), while increasing the field drives a sign reversal, marking a transition to out-of-plane magnetic anisotropy (OMA). This reorientation originates from an electric field induced redistribution of Ti 3d orbital occupations,

which alters the SOC contribution to the total anisotropy energy. Such \vec{E} controlled modulation of K_μ highlights the potential of Ti_2Si as a platform for tunable spintronic phenomena.

At $E = 0.4 \text{ V}/\text{\AA}$, the PDOS as shown in Fig. 2, reveals a clear field-induced redistribution of the Ti–3d states near the Fermi level, accompanied by changes in Ti–Si hybridization and local bond geometry. This electronic rearrangement modifies the relative strength of the competing superexchange channels, leading to a pronounced minimum in the magnitude of the ferromagnetic exchange interaction J . The magnetic anisotropy K_μ exhibits a similar nonmonotonic response: it increases with the applied field and reaches its maximum at $E = 0.4 \text{ V}/\text{\AA}$, after which it decreases but remains positive. This behavior reflects the enhanced occupation of Ti–3d states around E_F at moderate fields, which strengthens the out-of-plane anisotropy before weakening again at higher fields. Overall, the nonmonotonic evolution of both J and K_μ originates from the electric-field-driven reshaping of the Ti–3d electronic structure.

Overall, the \vec{E} dependent modulation of both J and K_μ

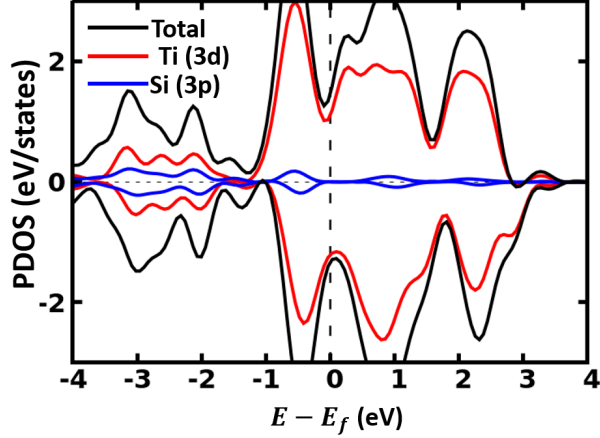


FIG. 2. Spin-resolved density of states of the Ti_2Si monolayer calculated under an applied electric field of 0.4 V/\AA .

demonstrates that Ti_2Si is a promising two-dimensional magnetic system with electrically controllable exchange and anisotropy energies. Such tunability suggests potential applications of Ti_2Si in voltage controlled spintronic and magnetoelectric devices. We have also explored the possibility of inducing inversion symmetry breaking in the Ti_2Si monolayer by applying an external electric field, aiming to generate a finite DMI. However, even under a relatively strong electric field of 0.8 V/\AA , the structural inversion symmetry remained preserved, as no significant atomic displacement or potential asymmetry was observed between the two Ti sublayers. This indicates that the intrinsic crystal field and strong covalent bonding in Ti-Si layers effectively screen the external perturbation, thereby suppressing \vec{E} driven inversion asymmetry and, consequently, the emergence of DMI.

B. Influence of Doping on Exchange interactions and magnetic anisotropy

Even when an external electric field is applied, the inversion symmetry of pristine Ti_2Si remains intact, preventing the formation of any finite DMI. To lift this intrinsic symmetry constraint and strengthen the magnetic interactions, we introduce Transition Metal (TM) substitution at the Ti sites. Co doping generates substantial local magnetic moments and enhances the exchange coupling, while Pt, owing to its strong SOC, supplies the relativistic contribution required to produce a finite DMI. The schematic illustration of Co and Pt doping in Ti_2Si monolayer is shown in Fig. 3 (a).

To investigate the combined influence of magnetism and SOC, we constructed a 4×2 Ti_2Si supercell and examined several substitutional configurations, including $\text{Pt}_{0.5}\text{Ti}_{1.5}\text{Si}$, $\text{Pt}_{0.5}\text{Co}_{0.5}\text{TiSi}$, $\text{Pt}_{0.5}\text{CoTi}_{0.5}\text{Si}$, and $\text{Pt}_1\text{Co}_{0.5}\text{Ti}_{0.5}\text{Si}$, together with the limiting cases CoTiSi , PtTiSi , and $\text{Pt}_{0.5}\text{Ti}_{1.5}\text{Si}$. Among these, only the $\text{Pt}_1\text{Co}_{0.5}\text{Ti}_{0.5}\text{Si}$ configuration is dynamically unstable, while all others remain stable, as con-

firmed in Fig. S1 of the Supplementary Material [53]. This systematic chemical substitution provides a controlled route to tune the balance between exchange interactions and SOC, offering a microscopic basis for identifying how each contribution influences the emergence and stabilization of chiral magnetic textures. The optimized atomic configuration of $\text{Pt}_{0.5}\text{CoTi}_{0.5}\text{Si}$ is illustrated in Fig. 3 (b), where Co and Pt atoms are distributed asymmetrically within a 4×2 supercell of Ti_2Si , thereby breaking local inversion symmetry and providing a natural environment for DMI to emerge.

Fig. 3 (c) shows the orbital-projected band structure of the $\text{Pt}_{0.5}\text{CoTi}_{0.5}\text{Si}$ configuration, revealing how TM substitution modifies the electronic states of the Ti_2Si host. The Pt-derived $5d$ states strongly hybridize with the Si $3p$ manifold in the energy window below the Fermi level, reflecting the substantial SOC introduced by Pt. In parallel, the Co $3d$ orbitals couple predominantly with the Ti $3d$ states, forming a broadened d -band complex that enhances the exchange-splitting within the magnetic sublattice. The coexistence of these two distinct types of hybridization, Pt-induced strong SOC on one side and Co driven magnetic exchange on the other breaks the local chemical environment and reshapes the low energy band dispersion. This asymmetric redistribution of orbital character provides the microscopic origin for the emergence of finite DMI in the doped Ti_2Si system, as it modifies both the relativistic hopping amplitudes and the exchange pathways responsible for chiral magnetic interactions.

The element-resolved magnetic moments listed in Table I show a clear dependence on the local Pt/Co/Ti coordination around the magnetic sites. In the Ti-rich composition $\text{Pt}_{0.5}\text{Ti}_{1.5}\text{Si}$, the Ti atoms carry a sizeable M_{Ti} of $1.24 \mu_B$, while Co is absent and Pt hosts only a very small induced moment of $0.02 \mu_B$, reflecting the weak polarization of Pt- $5d$ states. Introducing Co into the lattice, as in $\text{Pt}_{0.5}\text{Co}_{0.5}\text{TiSi}$, leads to the development of a substantial Co moment and a moderate Ti moment, indicating that the spin density becomes redistributed between Co and Ti through hybridization. The induced Pt moment also increases slightly, highlighting the sensitivity of Pt- $5d$ polarization to the presence of magnetic Co neighbors. Upon further increasing the Co concentration to $\text{Pt}_{0.5}\text{Co}_1\text{Ti}_{0.5}\text{Si}$, the Co moment reaches its maximum value ($1.55 \mu_B$), while the Ti moment drops significantly to $0.52 \mu_B$, demonstrating that the magnetic character becomes increasingly dominated by the Co network. The induced Pt moment is also largest in this composition ($0.06 \mu_B$), consistent with stronger Co-Pt hybridization. In the CoTiSi compound, the Co and Ti moments remain sizable, while in PtTiSi , where Co is absent, Ti retains a moderate moment ($0.89 \mu_B$) and Pt acquires only a small induced moment ($0.02 \mu_B$). Overall, the data reveal a systematic evolution of the magnetic moments: Ti carries the dominant moment in Ti-rich compositions, Co becomes the primary magnetic contributor as its concentration increases, and Pt consistently hosts only a small induced moment whose magnitude reflects the degree of Co-Pt hybridization. These trends highlight the interplay between local chemical coordination and the distribution of spin density across the Pt/Co/Ti sublattice.

To understand how the local chemical environment shapes

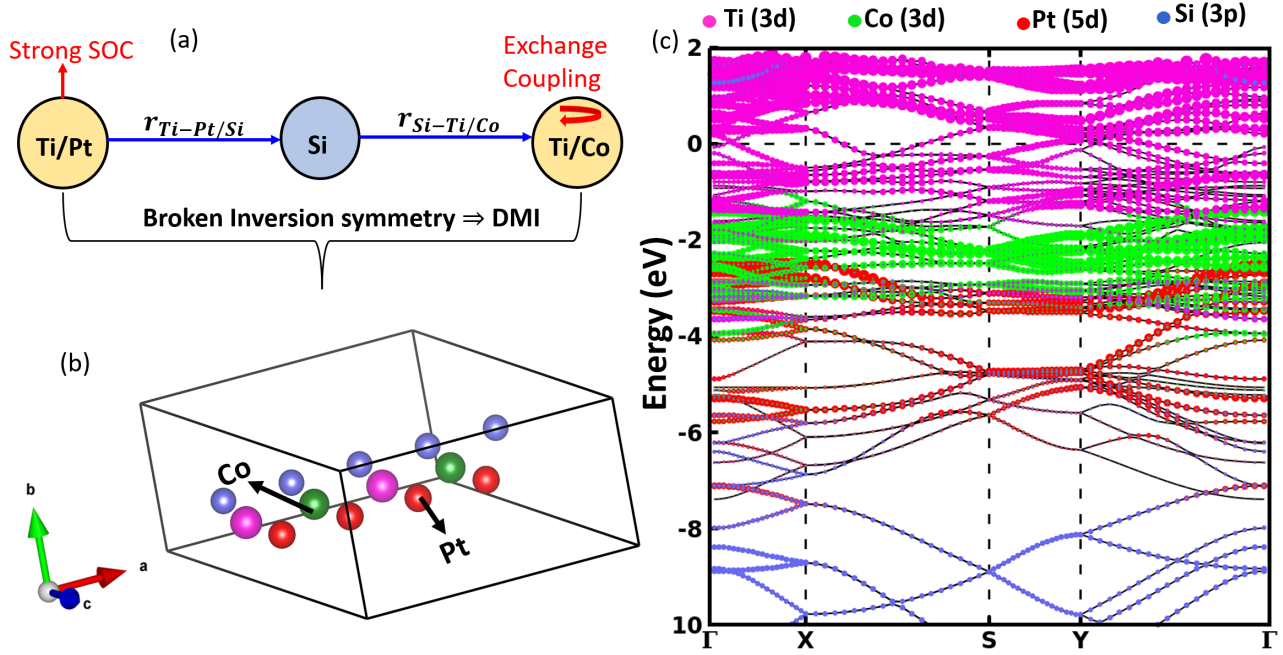


FIG. 3. (a) Schematic representation of the asymmetric Ti/Pt-Si-Ti/Co exchange pathway in the doped Ti_2Si monolayer. Pt provides strong SOC on one side and Co strengthens the exchange interaction on the other, together creating the conditions required for a finite DMI. (b) Relaxed atomic structure of the $\text{Pt}_{0.5}\text{CoTi}_{0.5}\text{Si}$ configuration, illustrating the asymmetric coordination created by simultaneous Pt and Co substitution. (c) Orbital-projected band structure of $\text{Pt}_{0.5}\text{CoTi}_{0.5}\text{Si}$ structure.

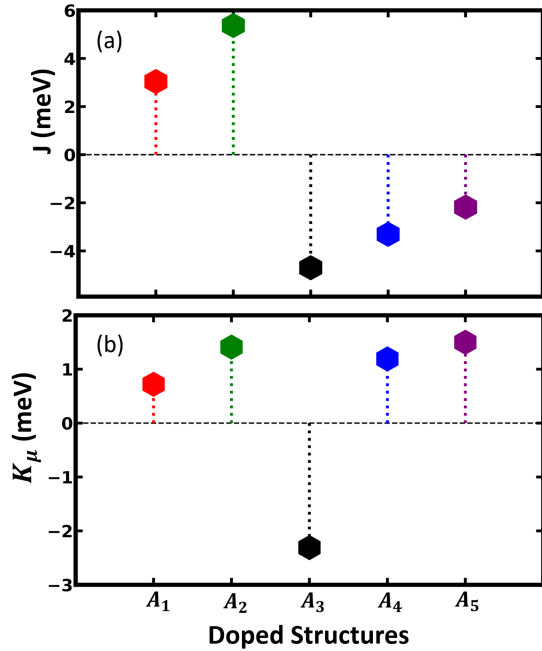


FIG. 4. Evolution of the (a) exchange interaction J and (b) magnetic anisotropy K_μ across different doped Ti_2Si configurations. The abbreviations correspond to: $A_1 = \text{Pt}_{0.5}\text{Ti}_{1.5}\text{Si}$, $A_2 = \text{Pt}_{0.5}\text{Co}_{0.5}\text{Ti}_1\text{Si}$, $A_3 = \text{Pt}_{0.5}\text{Co}_1\text{Ti}_{0.5}\text{Si}$, $A_4 = \text{CoTiSi}$, and $A_5 = \text{PtTiSi}$.

the magnetic behavior, we analyzed J and K_μ for the five $\text{Pt}_x\text{Co}_y\text{Ti}_z\text{Si}$ compositions listed in Table I, with the corresponding trends plotted in Figs. 4 (d)–(e). In the first two compositions, $\text{Pt}_{0.5}\text{Ti}_{1.5}\text{Si}$ and $\text{Pt}_{0.5}\text{Co}_{0.5}\text{Ti}_1\text{Si}$, both J and K_μ are positive, indicating that the exchange favors AFM alignment and that the magnetic easy axis lies out of the plane. In these compositions, the combined effect of Ti driven hybridization and SOC naturally favors OMA. When the Co concentration increases further, as in $\text{Pt}_{0.5}\text{Co}_1\text{Ti}_{0.5}\text{Si}$, the magnetic character changes significantly. Here, J becomes strongly negative, signaling the onset of FM coupling driven by enhanced Co-Co superexchange. At the same time, K_μ also turns negative, revealing a rotation of the OMA into IMA, consistent with the more planar bonding geometry around the closely spaced Co atoms. The two end-member compounds, CoTiSi and PtTiSi , likewise show negative J , yet retain positive K_μ , indicating that although FM exchange dominates, the anisotropy is still governed by the local Ti/Pt coordination and associated SOC. Overall, the trends demonstrate that the sign of J is controlled by the competition between Co-Ti hybridization, which favors AFM, and Co-Co superexchange, which favors FM. In contrast, the sign of K_μ reflects whether the local spin orbit environment stabilizes OMA or IMA.

TABLE I. Calculated element-resolved magnetic moments on Ti (M_{Ti}) and Co (M_{Co}), induced magnetic moment in Pt (M_{Pt}), nearest-neighbor exchange coupling J , single-ion anisotropy energy K_μ , DMI constants d_1 and d_2 , and corresponding Micromagnetic DMI strengths D_1 , D_2 for the different Pt/Co/Ti/Si compositions considered.

| Material | M_{Ti} (μ_B) | M_{Co} (μ_B) | M_{Pt} (μ_B) | J (meV) | K_μ (meV) | d_1 (meV) | d_2 (meV) | D_1 (mJ/m ²) | D_2 (mJ/m ²) |
|--|----------------------|----------------------|----------------------|-----------|---------------|-------------|-------------|----------------------------|----------------------------|
| Pt _{0.5} Ti _{1.5} Si | 1.24 | 0.00 | 0.02 | 3.04 | 0.72 | 0.03 | -0.12 | 0.05 | -0.23 |
| Pt _{0.5} Co _{0.5} Ti ₁ Si | 1.17 | 1.05 | 0.05 | 5.37 | 1.41 | 0.09 | -0.17 | 0.17 | -0.33 |
| Pt _{0.5} Co ₁ Ti _{0.5} Si | 0.52 | 1.55 | 0.06 | -4.70 | -2.31 | 0.11 | -0.26 | 0.21 | -0.50 |
| CoTiSi | 0.82 | 0.97 | 0.00 | -3.31 | 1.19 | -0.04 | 0.00 | 0.08 | 0.00 |
| PtTiSi | 0.89 | 0.00 | 0.02 | -2.18 | 1.50 | 0.00 | -0.02 | 0.00 | -0.04 |

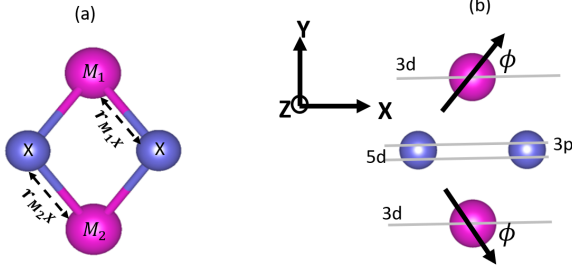


FIG. 5. (a) Schematic representation of a TM silicide, where M_1 and M_2 are magnetic transition-metal sites and X is a nonmagnetic ligand. (b) The minimal trimer model consisting of two magnetic sites, M_1 and M_2 , each hosting a d orbital, bridged by a nonmagnetic ligand X carrying either a p or d orbital. The magnetic moments on M_1 and M_2 are canted by an angle ϕ with respect to the x -axis.

C. Microscopic Origin of DMI: Tight-Binding Perspective

The third term of the Hamiltonian in Eq. 1 corresponds to DMI, which arises from SOC in systems without inversion symmetry and plays a crucial role in stabilizing chiral magnetic textures such as skyrmions [12, 54]. In the doped Ti₂Si lattice considered here, the top and bottom Ti layers are separated by a nonmagnetic Si spacer, while Pt/Co substitution breaks the horizontal mirror plane of the pristine Ti₂Si structure. Consequently, the system is both intralayer and interlayer asymmetric [55]:

- (1) Within each magnetic Ti (or Ti/Co) layer, local bond distortions generated by Pt/Co doping break inversion symmetry, giving rise to intralayer DMI; and
- (2) The two magnetic layers become chemically and structurally inequivalent, allowing a distinct interlayer DMI across the Si layer.

To understand the microscopic origin of the resulting non-collinear exchange, we construct a minimal TB Hamiltonian based on MLWFs [39]. The model is built on a trimer M_1 - X - M_2 cluster, where two magnetic sites M_1 and M_2 are bridged by a nonmagnetic ligand X , mimicking the Ti-Si-Ti link in the monolayer geometry [Fig. 5]. The TB Hamiltonian takes the form

$$\hat{H} = \hat{H}_0 + \hat{H}_t + \hat{H}_{\text{SOC}}, \quad (3)$$

where \hat{H}_0 contains the on-site energies, \hat{H}_t describes ligand-mediated hopping, and \hat{H}_{SOC} introduces SOC. The interplay

of SOC with the broken inversion symmetry in the asymmetric M_1 - X - M_2 geometry generates the antisymmetric exchange responsible for the DMI.

The on-site term corresponds to:

$$\hat{H}_0 = \sum_{im,\sigma} \epsilon_{d,m} d_{im\sigma}^\dagger d_{im\sigma} + \sum_{\alpha,\sigma} \epsilon_{p,\alpha} p_{\alpha\sigma}^\dagger p_{\alpha\sigma} + \sum_{\alpha,\sigma} \epsilon_{d,\alpha} d_{\alpha\sigma}^\dagger d_{\alpha\sigma} \quad (4)$$

where $\epsilon_{d,m}$ and $\epsilon_{p,\alpha}$ denote the on-site energies of the m -th M - d and α -th X - p (or X - d) orbitals. The operators $d_{m\sigma}^\dagger$ ($d_{m\sigma}$) and $p_{\alpha\sigma}^\dagger$ ($p_{\alpha\sigma}$) create (annihilate) an electron with spin σ in the corresponding orbitals. The ligand-mediated hopping between the magnetic and nonmagnetic sites is given by

$$\hat{H}_t = \sum_{i,m,\alpha,\sigma} \left(H_{m\alpha}^{(iX)} d_{im\sigma}^\dagger p_{\alpha\sigma} + H_{m\alpha}^{(iX)} d_{im\sigma}^\dagger d_{\alpha\sigma} + \text{h.c.} \right), \quad (5)$$

while SOC contributes via

$$\begin{aligned} \hat{H}_{\text{SOC}} = \lambda_X \sum_{\alpha,\beta,\sigma,\sigma'} & (p_{\alpha\sigma}^\dagger \langle p_\alpha | \mathbf{L} | p_\beta \rangle \cdot \langle \sigma | \mathbf{S} | \sigma' \rangle p_{\beta\sigma'} \\ & + d_{\alpha\sigma}^\dagger \langle d_\alpha | \mathbf{L} | d_\beta \rangle \cdot \langle \sigma | \mathbf{S} | \sigma' \rangle d_{\beta\sigma'}), \end{aligned} \quad (7)$$

with analogous terms on the metal sites.

From the Wannier representation, we extract the orbital-resolved hopping matrix elements for both Si and Pt ligands:

$$\begin{aligned} t_{m,\alpha}^{(M_1\text{Si})} &= \langle d_m^{(M_1)} | \hat{H} | p_\alpha^{(\text{Si})} \rangle, & t_{n,\beta}^{(M_2\text{Si})} &= \langle d_n^{(M_2)} | \hat{H} | p_\beta^{(\text{Si})} \rangle, \\ t_{m,\alpha}^{(M_1\text{Pt})} &= \langle d_m^{(M_1)} | \hat{H} | d_\alpha^{(\text{Pt})} \rangle, & t_{n,\beta}^{(M_2\text{Pt})} &= \langle d_n^{(M_2)} | \hat{H} | d_\beta^{(\text{Pt})} \rangle, \end{aligned} \quad (8)$$

where $m, n, \alpha, \beta \in \{xy, yz, xz, x^2 - y^2, z^2\}$ for d -type orbitals, and $\alpha, \beta \in \{x, y, z\}$ for p -type orbitals.

From the Wannier-based TB Hamiltonian, we extract all orbital-resolved hopping amplitudes t_{ij} between orbitals i and j . For each hopping channel, the associated geometric direction is defined as

$$\vec{\mathbf{R}} = \mathbf{a}_{\text{lat}} + (\mathbf{r}_i - \mathbf{r}_j), \quad (9)$$

where \mathbf{a}_{lat} connects the unit cells of the two orbitals, and $\mathbf{r}_i, \mathbf{r}_j$ denote their intracell coordinates. The corresponding hopping vector is then written as

$$\vec{\mathbf{R}}_{ij} = t_{ij} \vec{\mathbf{R}}, \quad (10)$$

which carries units of (eV \cdot Å) and encodes both the magnitude and the spatial orientation of the orbital couplings along the

M_1 - X - M_2 superexchange pathway, the microscopic origin of DMI.

Following Blügel [56], the emergence of antisymmetric exchange is governed by the noncollinearity of such hopping channels. For the M_1 - X - M_2 trimer, the site-dependent orbital moments $\vec{\theta}_i$ can be expressed as

$$\vec{\theta}_i = \theta_i(\cos\phi\hat{\mathbf{e}}_x \pm \sin\phi\hat{\mathbf{e}}_y),$$

where ϕ is the canting angle defined in Fig. 5(b). SOC and local inversion-symmetry breaking modify the orientation of the M_i - X hybrid orbitals, and the resulting hopping vectors may be represented as

$$\vec{\mathbf{R}}_{ij} = R_{ij}^x\hat{\mathbf{e}}_x \pm R_{ij}^y\hat{\mathbf{e}}_y,$$

with approximate magnitudes $|R_{ij}^x| \approx |\theta_i \cos\phi|$ and $|R_{ij}^y| \approx |\theta_i \sin\phi|$. Once all hopping vectors are expressed in a common global coordinate frame, the microscopic chirality of a given superexchange path is evaluated from the cross product of the hopping channels involving the ligand,

$$d_{ij}^{\text{TB}} \propto \mathbf{R}_{ik} \times \mathbf{R}_{kj}, \quad (11)$$

where $i \in M_1$, $j \in M_2$, and k labels the ligand orbital. This quantity has units of ($\text{eV}^2\text{\AA}^2$) but is used only as a dimensionless chirality indicator: its sign and relative magnitude reveal whether a particular M - X - M pathway supports finite antisymmetric exchange. It is directly analogous to the DMI term in Eq. 1, although it is not a physical DMI coefficient.

The TB model is constructed from Wannier90 derived hopping parameters [39], with SOC strengths. The TB eigenvalues and eigenfunctions are fitted to the DFT band structure, and excellent agreement is obtained for $\text{Pt}_{0.5}\text{Co}_{1.5}\text{Ti}_{0.5}\text{Si}$, as shown in Fig. S3 of the Supplementary Material [53]. This Wannier-based TB analysis identifies two distinct antisymmetric exchange paths: a weak Si-mediated channel and a dominant Pt-mediated interlayer channel. Using Eq. 11, we compute the chirality indicators for the Co-Si-Co, Co-Pt-Co, Ti-Si-Ti, and Ti-Pt-Ti paths (in both intralayer and interlayer geometries) across all Pt/Co-substituted Ti_2Si compositions. The results in Table II show that nonzero entries identify symmetry allowed chiral pathways, whereas the Ti-Si-Ti channel vanishes for all compositions except $\text{Pt}_{0.5}\text{Ti}_{1.5}\text{Si}$. This composition behaves differently because, in the absence of Co, only the weaker Ti-mediated pathways are active, yielding smaller DMI signatures compared to the Co-containing systems. The sign of d_{ij}^{TB} follows the right-hand convention, with positive (negative) values indicating CCW (CW) rotation around the $+\hat{z}$ ($-\hat{z}$) direction.

Density functional results. The TB model provides the microscopic chirality signatures, while the actual DMI vectors are obtained from a symmetry analysis of the real-space atomic geometry. Following Moriya's symmetry rules [49, 50], the DMI interaction between two magnetic atoms M_1 and M_2 located at sites i and j arises through the M_1 - X - M_2 superexchange pathways mediated by the nonmagnetic atom(s)

TABLE II. Tight-binding chirality indicators using Eq. 11 for the Co-Si-Co, Co-Pt-Co, Ti-Si-Ti, and Ti-Pt-Ti superexchange pathways in Pt/Co-substituted Ti_2Si . These quantities have units of ($\text{eV}^2\text{\AA}^2$) but are reported in arbitrary units, since only their sign and relative magnitude determine whether a given M_1 - X - M_2 pathway supports antisymmetric exchange.

| Material | Co-Si-Co | Co-Pt-Co | Ti-Si-Ti | Ti-Pt-Ti |
|--|----------|----------|----------|----------|
| $\text{Pt}_{0.5}\text{Ti}_{1.5}\text{Si}$ | 0.00 | 0.00 | -0.90 | -2.08 |
| $\text{Pt}_{0.5}\text{Co}_{0.5}\text{Ti}_1\text{Si}$ | 0.89 | -2.96 | -0.002 | 0.00 |
| $\text{Pt}_{0.5}\text{Co}_1\text{Ti}_{0.5}\text{Si}$ | 4.38 | -6.44 | -0.00 | 0.00 |
| CoTiSi | -1.68 | 0.00 | 0.00 | 0.00 |
| PtTiSi | 0.00 | 0.00 | 0.00 | 0.00 |

X , as illustrated in Fig. 5. For each exchange path, the corresponding DMI vector takes the minimal symmetry-allowed form:

$$\vec{d}_{ij} = d_{ij}(\hat{r}_{iX} \times \hat{r}_{jX}), \quad (12)$$

where \hat{r}_{iX} and \hat{r}_{jX} are the unit vectors from the mediating atom X toward the magnetic sites i and j . As illustrated in Fig. 6 (a), the present geometry contains two symmetry related M_1 - X - M_2 pathways, giving rise to two independent DMI vectors: \vec{d}_1 , which originates predominantly from the Si-mediated intralayer and interlayer exchange, and \vec{d}_2 , which is dominated by the Pt-mediated interlayer interaction.

The layer-resolved DMI constants are extracted using the spin-spiral method, where each component (\vec{d}_1 or \vec{d}_2) is obtained from the energy difference between clockwise (CW) and counterclockwise (CCW) spirals,

$$d = \frac{E_{\text{CW}} - E_{\text{CCW}}}{m},$$

with m denoting the number of chiral magnetic bonds participating in the imposed spiral. The CW and CCW spin-spiral configurations used to extract the DMI constants are shown in Fig. 6 (b) - (c). Since the structural models for the doped systems are already constructed using a 4×2 supercell, no additional supercell is required for the DMI calculations. Where $m = 16$ for the Si mediated DMI vector \vec{d}_1 , and $m = 2\sqrt{2}$ for the Pt mediated interlayer DMI vector \vec{d}_2 , as derived in Sec. IV of the Supplementary Material [53].

The resulting DMI vectors \vec{d}_1 and \vec{d}_2 are illustrated in Fig. 6 (d) - (e), and their magnitudes are summarized in Table I. A clear hierarchy emerges: \vec{d}_2 is consistently and substantially larger than \vec{d}_1 , reflecting the much stronger SOC on Pt and the more efficient chiral exchange it mediates across the spacer. This trend is fully consistent with our TB analysis, which shows that the Co-Pt-Co exchange channel carries a much larger antisymmetric DMI exchange energy compared to the Ti-Si-Ti channel as shown in Table II. For Pt containing compositions such as $\text{Pt}_{0.5}\text{Ti}_{1.5}\text{Si}$, $\text{Pt}_{0.5}\text{Co}_{0.5}\text{Ti}_1\text{Si}$, and $\text{Pt}_{0.5}\text{Co}_1\text{Ti}_{0.5}\text{Si}$, the Pt assisted interlayer DMI dominates the total chiral interaction, in agreement with the TB prediction that Co-Pt-Co couplings exhibit the strongest SOC-induced asymmetry. In contrast, Si-mediated DMI remains weak: in

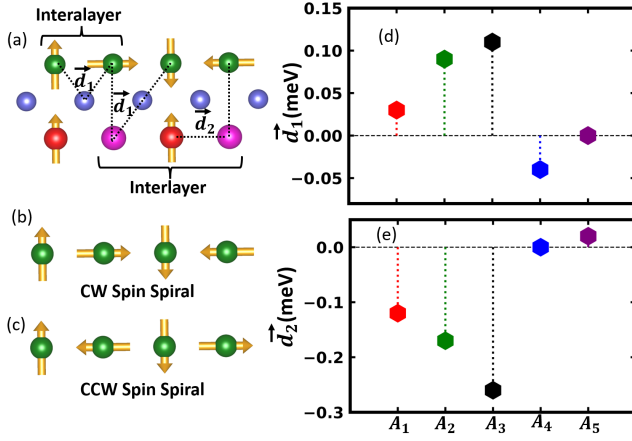


FIG. 6. (a) Schematic illustration of the two symmetry-allowed DMI pathways in doped Ti_2Si . The first pathway, \vec{d}_1 , contains both intralayer and weak interlayer contributions transmitted primarily through Si and Pt, whereas the second pathway, \vec{d}_2 , is a predominantly interlayer DMI mediated by Pt. (b) - (c) show the clockwise (CW) and Counterclockwise (CCW) spin spirals configurations. (d) and (e) Evolution of the calculated d_1 and d_2 values, respectively, for the configurations $A_1 = \text{Pt}_{0.5}\text{Ti}_{1.5}\text{Si}$, $A_2 = \text{Pt}_{0.5}\text{Co}_{0.5}\text{Ti}_1\text{Si}$, $A_3 = \text{Pt}_{0.5}\text{Co}_1\text{Ti}_{0.5}\text{Si}$, $A_4 = \text{CoTiSi}$, and $A_5 = \text{PtTiSi}$.

CoTiSi , the absence of Pt leads to a small \vec{d}_1 due to Co-Si-Co consistent with TB results as shown in Table II and vanishing \vec{d}_2 . Even in PtTiSi (where Co is absent), the Pt-mediated long-range pathway produces a very small but finite DMI contribution, $d_2 = -0.02$, while the Si-mediated term d_1 essentially vanishes. The corresponding TB chirality indicators for this composition appear nearly zero, reflecting the fact that both channels are extremely weak and fall below the TB model's numerical resolution. Nevertheless, the sign of the finite DFT-derived d_2 remains consistent with the general TB trend that the Pt-mediated exchange is intrinsically stronger than the Si-mediated one. Taken together, these results demonstrate that Pt driven interlayer DMI is the primary source of chirality in doped Ti_2Si , while Si-mediated intralayer and interlayer contributions are intrinsically weak.

In the micromagnetic limit, the discrete lattice spins \vec{S}_i are replaced by a continuous magnetization field $\vec{m}(\mathbf{r})$. Under this transformation, the DMI contribution arising from the third term of the Hamiltonian in Eq. 1 can be expressed as

$$E_{\text{DMI}} = \int d\mathbf{r} \varepsilon_{\text{DMI}} = \int d\mathbf{r} \sum_{\mu} D_{\mu} [\vec{m} \times \partial_{\mu} \vec{m}], \quad (13)$$

where $\varepsilon_{\text{DMI}} = \sum_{\mu} D_{\mu} (\vec{m} \times \partial_{\mu} \vec{m})$ is the micromagnetic DMI energy density, ∂_{μ} denotes the spatial derivative along direction μ , and D_{μ} is the corresponding micromagnetic DMI vector. For interfacial systems, this expression reduces to the widely used form [7, 57–59]

$$E_{\text{DMI}} = \int d\mathbf{r} D [\hat{\mathbf{m}} \cdot (\nabla \times \hat{\mathbf{m}}) - (\hat{\mathbf{m}} \cdot \nabla) \hat{\mathbf{m}}] \cdot \hat{\mathbf{z}}, \quad (14)$$

where D is the effective interfacial micromagnetic DMI con-

stant.

The micromagnetic coefficients D_1 and D_2 are connected to their corresponding atomistic DMI vectors \vec{d}_1 and \vec{d}_2 (derived in Supplementary [53] Sec. V; see Eqs. S25 and S29) through

$$D_1 = \frac{d_1 N}{at}, \quad (15)$$

$$D_2 = \frac{d_2 N}{at}, \quad (16)$$

where N is the number of magnetic atoms per unit cell, a is the in-plane lattice parameter, and t is the monolayer thickness. The extracted micromagnetic DMI values are listed in Table I.

Among all compositions, $\text{Pt}_{0.5}\text{Co}_1\text{Ti}_{0.5}\text{Si}$ exhibits the strongest chiral interaction, with $D_1 = 0.21 \text{ mJ/m}^2$ and $D_2 = -0.50 \text{ mJ/m}^2$. The opposite signs of D_1 and D_2 reflect their distinct rotational preferences: D_1 favors a CCW spin spiral, whereas D_2 favors a CW spiral, consistent with the conventions used in Eqs. 15 and 16. $\text{Pt}_{0.5}\text{Co}_{0.5}\text{Ti}_1\text{Si}$ likewise displays finite chirality, with $D_1 = 0.17 \text{ mJ/m}^2$ (CCW) and $D_2 = -0.33 \text{ mJ/m}^2$ (CW). These results show that both intralayer (Si-mediated) and interlayer (Si- and Pt-mediated) exchange pathways contribute to the total DMI, with the Pt-assisted path dominant in magnitude. The rotation senses extracted from D_1 and D_2 are also fully consistent with the TB chirality analysis as shown in Table II. Overall, the atomistic and micromagnetic results demonstrate that Pt-driven interlayer DMI is the primary source of chiral exchange in doped Ti_2Si , whereas the Si-mediated intralayer contribution remains intrinsically weak. This establishes Ti_2Si monolayers with controlled Pt and Co substitution as a robust platform for engineering sizable and tunable DMI, enabling the stabilization of chiral spin textures in centrosymmetry broken 2D TMS.

IV. CONCLUSION

In summary, we have combined density-functional theory, micromagnetic analysis, and Wannier-based tight-binding modeling to uncover the conditions under which monolayer Ti_2Si can host chiral magnetic interactions. The pristine material is a ferromagnetic metal whose exchange coupling and magnetic anisotropy can be tuned by an external electric field, but the underlying inversion symmetry prevents the formation of DMI. By introducing controlled Pt and Co substitution at Ti sites, we break the horizontal mirror symmetry of the Ti–Si–Ti trilayer and simultaneously enhance both magnetic exchange (via Co) and SOC (via Pt). This chemical asymmetry generates a robust DMI, dominated by a Pt-mediated interlayer superexchange channel, as confirmed by first-principles spiral calculations and independently by a TB chirality analysis. The strongest DMI occurs in the $\text{Pt}_{0.5}\text{CoTi}_{0.5}\text{Si}$ composition, where both intralayer favours CCW spin spiral rotation and interlayer paths consistently favor a CW rotation sense. Overall, our results demonstrate that substitutional doping provides an effective, experimentally accessible route to engineer sizable

and tunable DMI in doped 2D silicides. Ti_2Si -based monolayers thus constitute a promising platform for realizing electri-

cally controllable chiral spin textures and for developing next-generation 2D spintronic devices.

-
- [1] A. N. Bogdanov and D. Yablonskii, *Zh. Eksp. Teor. Fiz* **95**, 178 (1989), URL [https://doi.org/10.1016/0304-8853\(94\)90046-9](https://doi.org/10.1016/0304-8853(94)90046-9).
 - [2] X. Wang, D. Sheng Wang, R. Wu, and A. Freeman, *Journal of Magnetism and Magnetic Materials* **159**, 337 (1996), ISSN 0304-8853, URL <https://www.sciencedirect.com/science/article/pii/S0304885395009361>.
 - [3] M. Heide, G. Bihlmayer, and S. Blügel, *Phys. Rev. B* **78**, 140403 (2008), URL <https://link.aps.org/doi/10.1103/PhysRevB.78.140403>.
 - [4] Z. Shen, C. Song, Y. Xue, Z. Wu, J. Wang, and Z. Zhong, *Phys. Rev. B* **106**, 094403 (2022), URL <https://link.aps.org/doi/10.1103/PhysRevB.106.094403>.
 - [5] C. Gong, L. Li, Z. Li, H. Ji, A. Stern, Y. Xia, T. Cao, W. Bao, C. Wang, Y. Wang, et al., *Nature* **546**, 265 (2017), URL <https://doi.org/10.1038/nature22060>.
 - [6] K. S. Burch, D. Mandrus, and J.-G. Park, *Nature* **563**, 47 (2018).
 - [7] A. Fert, V. Cros, and J. Sampaio, *Nature nanotechnology* **8**, 152 (2013), URL <https://doi.org/10.1038/nnano.2013.29>.
 - [8] S. Mühlbauer, B. Binz, F. Jonietz, C. Pfleiderer, A. Rosch, A. Neubauer, R. Georgii, and P. Böni, *Science* **323**, 915 (2009), <https://www.science.org/doi/pdf/10.1126/science.1166767>, URL <https://www.science.org/doi/abs/10.1126/science.1166767>.
 - [9] X. Yu, N. Kanazawa, Y. Onose, K. Kimoto, W. Zhang, S. Ishiwata, Y. Matsui, and Y. Tokura, *Nature materials* **10**, 106 (2011), URL <https://doi.org/10.1038/nmat2916>.
 - [10] E. Ruff, P. Lunkenheimer, A. Loidl, H. Berger, and S. Krohns, *Scientific reports* **5**, 15025 (2015), URL <https://www.nature.com/articles/srep15025>.
 - [11] O. L. Makarova, A. V. Tsvyashchenko, G. Andre, F. Porcher, L. N. Fomicheva, N. Rey, and I. Mirebeau, *Phys. Rev. B* **85**, 205205 (2012), URL <https://link.aps.org/doi/10.1103/PhysRevB.85.205205>.
 - [12] Y. Zhou, *National Science Review* **6**, 210 (2018), ISSN 2095-5138, <https://academic.oup.com/nsr/article-pdf/6/2/210/38915382/nwy109.pdf>, URL <https://doi.org/10.1093/nsr/nwy109>.
 - [13] Y. Gao, S. Yan, Q. Yin, H. Huang, Z. Li, Z. Zhu, J. Cai, B. Shen, H. Lei, Y. Zhang, et al., *Phys. Rev. B* **105**, 014426 (2022), URL <https://link.aps.org/doi/10.1103/PhysRevB.105.014426>.
 - [14] D. J. O'Hara, T. Zhu, A. H. Trout, A. S. Ahmed, Y. K. Luo, C. H. Lee, M. R. Brenner, S. Rajan, J. A. Gupta, D. W. McComb, et al., *Nano Letters* **18**, 3125 (2018), PMID: 29608316, <https://doi.org/10.1021/acs.nanolett.8b00683>, URL <https://doi.org/10.1021/acs.nanolett.8b00683>.
 - [15] D. Rani, B. R. K. Nanda, and P. Samal, *Phys. Rev. B* **112**, 174401 (2025), URL <https://link.aps.org/doi/10.1103/jj81-ng8g>.
 - [16] Y. Ga, Q. Cui, J. Liang, D. Yu, Y. Zhu, L. Wang, and H. Yang, *Phys. Rev. B* **106**, 054426 (2022), URL <https://link.aps.org/doi/10.1103/PhysRevB.106.054426>.
 - [17] L. Webster and J.-A. Yan, *Phys. Rev. B* **98**, 144411 (2018), URL <https://link.aps.org/doi/10.1103/PhysRevB.98.144411>.
 - [18] B. L. Chittari, Y. Park, D. Lee, M. Han, A. H. MacDonald, E. Hwang, and J. Jung, *Phys. Rev. B* **94**, 184428 (2016), URL <https://link.aps.org/doi/10.1103/PhysRevB.94.184428>.
 - [19] J. Liang, W. Wang, H. Du, A. Hallal, K. Garcia, M. Chshiev, A. Fert, and H. Yang, *Phys. Rev. B* **101**, 184401 (2020), URL <https://link.aps.org/doi/10.1103/PhysRevB.101.184401>.
 - [20] M. Haim, A. Levchenko, and M. Khodas, *Phys. Rev. B* **105**, 024515 (2022), URL <https://link.aps.org/doi/10.1103/PhysRevB.105.024515>.
 - [21] A. Ghosh, S. Jana, M. Hossain, D. Rani, S. Śmiga, and P. Samal, *Phys. Rev. B* **112**, 045128 (2025), URL <https://link.aps.org/doi/10.1103/8vvn-k9p3>.
 - [22] X. Sui, T. Hu, J. Wang, B.-L. Gu, W. Duan, and M.-s. Miao, *Phys. Rev. B* **96**, 041410 (2017), URL <https://link.aps.org/doi/10.1103/PhysRevB.96.041410>.
 - [23] Z. Shen, C. Song, Y. Xue, Z. Wu, J. Wang, and Z. Zhong, *Phys. Rev. B* **106**, 094403 (2022), URL <https://link.aps.org/doi/10.1103/PhysRevB.106.094403>.
 - [24] J. Liang, W. Wang, H. Du, A. Hallal, K. Garcia, M. Chshiev, A. Fert, and H. Yang, *Phys. Rev. B* **101**, 184401 (2020), URL <https://link.aps.org/doi/10.1103/PhysRevB.101.184401>.
 - [25] Q. Cui, J. Liang, Z. Shao, P. Cui, and H. Yang, *Phys. Rev. B* **102**, 094425 (2020), URL <https://link.aps.org/doi/10.1103/PhysRevB.102.094425>.
 - [26] C. Moreau-Luchaire, C. Moutafis, N. Reyren, J. Sampaio, C. Vaz, N. Van Horne, K. Bouzehouane, K. Garcia, C. Deranlot, P. Warnicke, et al., *Nature nanotechnology* **11**, 444 (2016), URL <https://doi.org/10.1038/nnano.2015.313>.
 - [27] S. Heinze, K. Von Bergmann, M. Menzel, J. Brede, A. Kubetzka, R. Wiesendanger, G. Bihlmayer, and S. Blügel, *nature physics* **7**, 713 (2011), URL <https://doi.org/10.1038/nphys2045>.
 - [28] S. Emori, U. Bauer, S.-M. Ahn, E. Martinez, and G. S. Beach, *Nature materials* **12**, 611 (2013), URL <https://doi.org/10.1038/nmat3675>.
 - [29] X. Chen and C. Liang, *Catal. Sci. Technol.* **9**, 4785 (2019), URL <http://dx.doi.org/10.1039/C9CY00533A>.
 - [30] H. Ihou Mouko, K. Romanjek, M. Mejri, M. Oulfarsi, S. El Oualid, P. Malinconi, Y. Thimont, B. Malard, C. Estournès, N. David, et al., *Energy Conversion and Management* **242**, 114304 (2021), ISSN 0196-8904, URL <https://www.sciencedirect.com/science/article/pii/S0196890421004805>.
 - [31] W. S. Yun, G.-B. Cha, and S. C. Hong, *Journal of Magnetism and Magnetic Materials* **304**, e31 (2006), ISSN 0304-8853, international Symposium on Spintronics and Advanced Magnetic Technologies and International Symposium on Magnetic Materials and Applications 2005, URL <https://www.sciencedirect.com/science/article/pii/S030488530600223X>.
 - [32] A. Kumar, P. Singh, A. Doyle, D. L. Schlagel, and Y. Mudryk, *Phys. Rev. B* **109**, 214410 (2024), URL <https://link.aps.org/doi/10.1103/PhysRevB.109.214410>.

- [33] E. A. Karhu, U. K. Röbber, A. N. Bogdanov, S. Kahwaji, B. J. Kirby, H. Fritzsche, M. D. Robertson, C. F. Majkrzak, and T. L. Monchesky, Phys. Rev. B **85**, 094429 (2012), URL <https://link.aps.org/doi/10.1103/PhysRevB.85.094429>.
- [34] A. O. Leonov, I. M. Tambovtcev, I. S. Lobanov, and V. M. Uzdin, Phys. Rev. B **102**, 174415 (2020), URL <https://link.aps.org/doi/10.1103/PhysRevB.102.174415>.
- [35] Q. Wu, J.-J. Zhang, P. Hao, Z. Ji, S. Dong, C. Ling, Q. Chen, and J. Wang, The Journal of Physical Chemistry Letters **7**, 3723 (2016), pMID: 27603004, <https://doi.org/10.1021/acs.jpclett.6b01731>, URL <https://doi.org/10.1021/acs.jpclett.6b01731>.
- [36] X. Lan, L. Yu, X. Lv, and F. Li, physica status solidi (RRL)–Rapid Research Letters **15**, 2100048 (2021).
- [37] H. Yang, A. Thiaville, S. Rohart, A. Fert, and M. Chshiev, Phys. Rev. Lett. **115**, 267210 (2015), URL <https://link.aps.org/doi/10.1103/PhysRevLett.115.267210>.
- [38] V. Borisov, Q. Xu, N. Ntallis, R. Clulow, V. Shtender, J. Cederwall, M. Sahlberg, K. T. Wikfeldt, D. Thonig, M. Pereiro, et al., Phys. Rev. Mater. **6**, 084401 (2022), URL <https://link.aps.org/doi/10.1103/PhysRevMaterials.6.084401>.
- [39] G. Pizzi, V. Vitale, R. Arita, S. Blügel, F. Freimuth, G. Géranton, M. Gibertini, D. Gresch, C. Johnson, T. Koretsune, et al., Journal of Physics: Condensed Matter **32**, 165902 (2020), URL <https://iopscience.iop.org/article/10.1088/1361-648X/ab51ff>.
- [40] A. A. Mostofi, J. R. Yates, Y.-S. Lee, I. Souza, D. Vanderbilt, and N. Marzari, Computer Physics Communications **178**, 685 (2008), ISSN 0010-4655, URL <https://www.sciencedirect.com/science/article/pii/S0010465507004936>.
- [41] G. Kresse and J. Furthmüller, Computational materials science **6**, 15 (1996).
- [42] G. Kresse and J. Furthmüller, Physical review B **54**, 11169 (1996).
- [43] G. Kresse and D. Joubert, Physical review b **59**, 1758 (1999).
- [44] J. P. Perdew, K. Burke, and M. Ernzerhof, Physical review letters **77**, 3865 (1996).
- [45] S. L. Dudarev, G. A. Botton, S. Y. Savrasov, C. J. Humphreys, and A. P. Sutton, Phys. Rev. B **57**, 1505 (1998), URL <https://link.aps.org/doi/10.1103/PhysRevB.57.1505>.
- [46] A. Togo and I. Tanaka, Scripta Materialia **108**, 1 (2015), ISSN 1359-6462, URL <https://www.sciencedirect.com/science/article/pii/S1359646215003127>.
- [47] H. J. Xiang, E. J. Kan, S.-H. Wei, M.-H. Whangbo, and X. G. Gong, Phys. Rev. B **84**, 224429 (2011), URL <https://link.aps.org/doi/10.1103/PhysRevB.84.224429>.
- [48] P. W. Anderson, Phys. Rev. **115**, 2 (1959), URL <https://link.aps.org/doi/10.1103/PhysRev.115.2>.
- [49] A. Fert and P. M. Levy, Phys. Rev. Lett. **44**, 1538 (1980), URL <https://link.aps.org/doi/10.1103/PhysRevLett.44.1538>.
- [50] T. Moriya, Phys. Rev. **120**, 91 (1960), URL <https://link.aps.org/doi/10.1103/PhysRev.120.91>.
- [51] A. P. Sutton, M. W. Finnis, D. G. Pettifor, and Y. Ohta, Journal of Physics C: Solid State Physics **21**, 35 (1988).
- [52] D. Gresch, Q. Wu, G. W. Winkler, R. Häuselmann, M. Troyer, and A. A. Soluyanov, Phys. Rev. Mater. **2**, 103805 (2018), URL <https://link.aps.org/doi/10.1103/PhysRevMaterials.2.103805>.
- [53] *See supplemental material at [url will be inserted by publisher] for details of phonon dispersion of doped structures, the derivative of magnetic parameters, tight binding band structure, dmi (intralayer and interlayer contribution), the micromagnetic dmi d* (2025).
- [54] S. Hasan, S. San, K. Baral, N. Li, P. Rulis, and W.-Y. Ching, Materials **15**, 2843 (2022).
- [55] T. Matthies, L. Rózsa, L. Szunyogh, R. Wiesendanger, and E. Y. Vedmedenko, Phys. Rev. Res. **6**, 043158 (2024), URL <https://link.aps.org/doi/10.1103/PhysRevResearch.6.043158>.
- [56] V. Kashid, T. Schena, B. Zimmermann, Y. Mokrousov, S. Blügel, V. Shah, and H. G. Salunke, Phys. Rev. B **90**, 054412 (2014), URL <https://link.aps.org/doi/10.1103/PhysRevB.90.054412>.
- [57] J. Iwasaki, M. Mochizuki, and N. Nagaosa, Nature nanotechnology **8**, 742 (2013), URL <https://doi.org/10.1038/nnano.2013.176>.
- [58] J. Sampaio, V. Cros, S. Rohart, A. Thiaville, and A. Fert, Nature nanotechnology **8**, 839 (2013), URL <https://doi.org/10.1038/nnano.2013.210>.
- [59] H. Yang, J. Liang, and Q. Cui, Nature Reviews Physics **5**, 43 (2023), URL <https://doi.org/10.1038/s42254-022-00529-0>.